frontiers | Frontiers in Earth Science

TYPE Original Research
PUBLISHED 16 August 2024
DOI 10.3389/feart.2024.1437012

EDITED BY
Gang Rao,
Southwest Petroleum University, China

REVIEWED BY
Yiduo Liu,
Chinese Academy of Sciences (CAS), China
Hu Wang,
Southwest Jiaotong University, China

*CORRESPONDENCE
Weimin He,
wmhe65@163.com

RECEIVED 23 May 2024
ACCEPTED 02 August 2024
PUBLISHED 16 August 2024

CITATION
Wei L, He W, Xu Y, Du Y, Dai A, Song X, Xu S and Qin J (2024) Late Quaternary activity of Wulashan Northern fault, North China.
Front. Earth Sci. 12:1437012.
doi: 10.3389/feart.2024.1437012

Late Quaternary activity of Wulashan Northern fault, North China

Leihua Wei[1], Weimin He[1]*, Yueren Xu[2], Yanlin Du[1], Aopeng Dai[1], Xiaopeng Song[1], Shuya Xu[1] and Jingjing Qin[1]

[1]Geophysical Exploration Center, China Earthquake Administration, Zhengzhou, China, [2]Institute of Earthquake Forecasting, China Earthquake Administration, Beijing, China

The Late Quaternary activity characteristics of secondary faults located between the main active faults at the boundaries of large basins are of great significance to the overall understanding of regional seismic hazards. The Wulashan Northern Fault (WNF) is located on the northern side of the Ordos Block, within the Northern Margin Fault Basin in North China, between the Sertengshan Piedmont Fault and Daqingshan Piedmont Fault. Current research on the geometry and kinematics of the WNF needs to be improved. In this study, we aimed to determine the shallow structural characteristics and Late Quaternary activity of the WNF using shallow seismic exploration and composite drilling geological cross-sectional analysis. The results indicate that the WNF is not a single surface fault but multiple branches with a northward-dipping stepped surface distribution. The latest activity of the F1 branch with a maximum coseismic vertical dislocation of 0.9 m occurred before 47.08 ± 3.7 ka B.P. The latest and older activities of the branch of F2 with a maximum coseismic vertical dislocation of 0.96 m and 1.15 m occurred before 73.8 ± 2.8 ka B.P. and 91.2 ± 4.4 ka B.P., respectively. According to a series of empirical relationships between length of surface rupture and magnitude, the maximum potential magnitude of the earthquake was determined to be M = 6.5–7.0. We argue that even though the Late Quaternary activity of the WNF was weaker than that of the other boundary faults of the Hetao Basin, the local urban and rural planning and land and resources construction in the Hetao Basin region should pay attention to the seismic risk of the WNF as an independent section in the future for the effect of secular tectonic loading.

KEYWORDS

Ordos block, Wulashan northern fault, shallow seismic exploration, composite drilling geological section, late Pleistocene activity

1 Introduction

The Ordos Block was essential for the Cenozoic and modern tectonic movements in North China. It was an important transitional area adjacent to the northeastern edge of the Tibetan Plateau (Zhang et al., 2003). The internal structural deformation and seismic activity of the block were weak. Owing to the expansion and compression of the Tibetan Plateau in the northeastern direction, and the sinking and stretching of the North China Block, the periphery of the Ordos Block is surrounded by a series of faults and fault basins, that is, the Hetao Basin, Shanxi Rift System

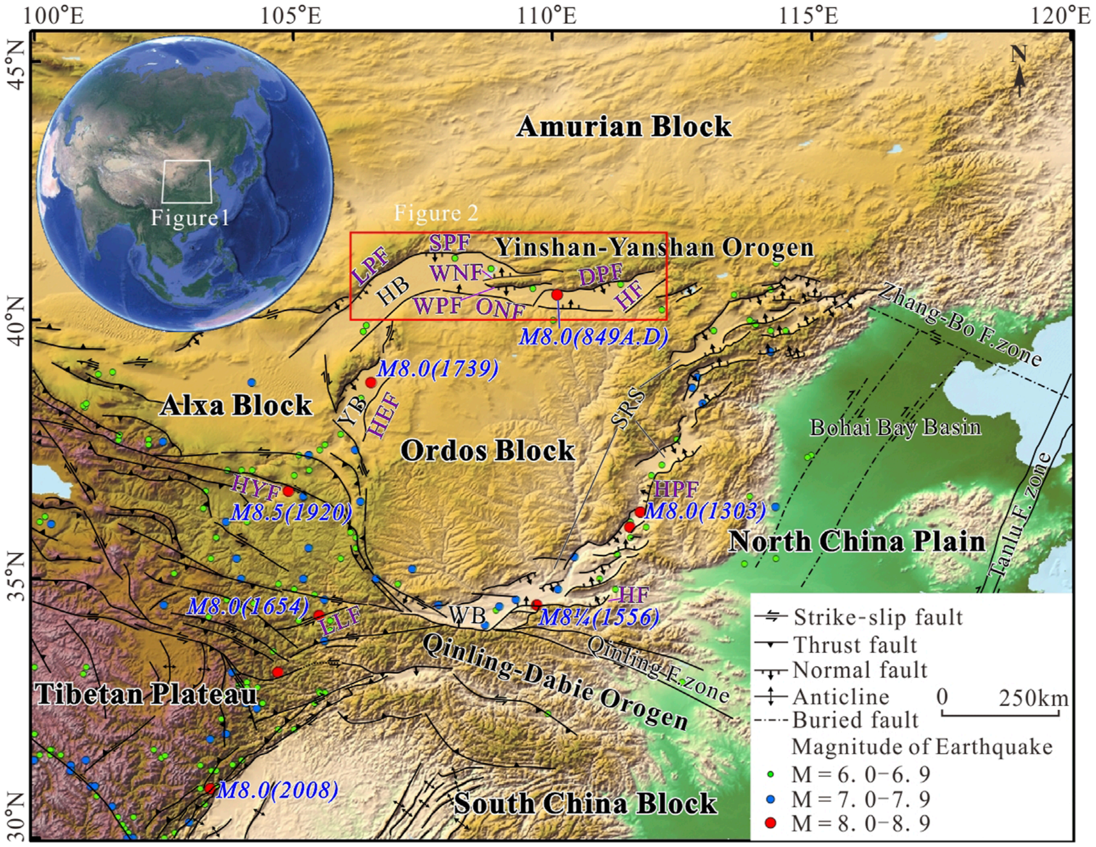

Abbreviations: WB, Weihe Basin; YB, Yinchuan Basin; HB, Hetao Basin; SRS, Shanxi Rift System. LPF, Langshan Piedmont Fault; SPF, Sertengshan Piedmont Fault; DPF, Daqingshan Piedmont Fault; ONF, Ordos Northern Fault; HF, Horiger Fault; WPF, Wulashan Piedmont Fault; WNF, Wulashan Northern Fault; HEF, Helanshan Eastern Fault; HF, Huashan Fault; LLF,Lixian-Luojiabu Fault; HYF, Haiyuan Fault; HPF, Huoshan Piedmont Fault.

FIGURE 1
Structures of the rift basins around the Ordos Block (modified after Su et al., 2023).

(SRS), Weihe Basin (WB), and Yinchuan Basin, from the northern edge in a clockwise direction (The Research Group on Active Fault System around Ordos Massif, 1988; Deng et al., 1999; Wang et al., 2001). Except for the Hetao Basin, The four fault basins experienced many disastrous earthquakes with $M \geq 7$, five of which had $M = 8.0$ or even more significant in history (Figure 1). The strong earthquakes have caused devastating disasters to people and the economy around each epicenter, such as the 1739 A.D. $M = 8.0$ Pingluo earthquake in the Yinchuan Basin (The Research Group on Active Fault System around Ordos Massif, 1988; Zhang et al., 1990; Wang et al., 2001).

The Hetao Basin is a Cenozoic faulted basin located among the Ordos Block, Alxa Block, and Yinshan-Yanshan Orogen, bounded by well-developed faults (Figure 1). From west to east, the northern boundary faults of the basin are the Langshan Piedmont Fault (LPF), Sertengshan Piedmont Fault (SPF), Wulashan Northern Fault (WNF), Wulashan Piedmont Fault (WPF), and Daqingshan Piedmont Fault (DPF). The Ordos Northern Fault (ONF) and Horiger Fault (HF) represent the southern and Eastern boundaries of the Hetao Basin, respectively. Affected by the NE expansion of the Tibetan Plateau and the subduction of the Pacific Plate, these faults had intense activity in the Quaternary, especially the northern boundary faults, which caused a series of strong earthquakes, instancing historical $M = 8.0$ earthquake occurred in 849 A.D. (Ran et al., 2003a; He et al., 2007; Nie et al., 2010; Nie, 2013; He and Ma, 2015; Rao et al., 2019; Su et al., 2021) (Figure 1). Future large earthquakes potentially threaten the area controlled by the northern boundary faults.

Over the last 40 years, scholars have extensively studied the characteristics of the Late Quaternary activity, vigorous earthquake activity, and seismic risk of those northern boundary faults, which provide insights into active structures and recurrence patterns of local strong earthquakes along active faults (Ma et al., 1998; Ma et al., 2000; Deng et al., 1999; Jiang et al., 2001; Ran et al., 2002, 2003b; Yang et al., 2002; Yang et al., 2003; Nie et al., 2011; Rao et al., 2016; Rao et al., 2019; Liang et al., 2019; He et al., 2020). More recent results showed that the LPF-SPF experienced seven paleoearthquakes during the Holocene, with a recurrence period of 1.37 ± 0.11 ka and an earthquake risk of $M > 8.0$ (Dong, 2016; Dong, 2016; Liang et al., 2021; Ma and Dong, 2024). The fourteen paleoearthquake events occurred during the Holocene in the DPF, including the 849 A.D. earthquake (Li et al., 2015; Yuan et al., 2023). Similarly, the WPF has experienced six paleoearthquakes during the Holocene (Li, 2014). However, research on the geometry and kinematics behaviors of the WNF is lacking. The Wulashan Piedmont Fault is the boundary fault of the secondary Sag within the Hetao Basin, located between the LPF-SPF and DPF. Obtaining information about the shallow structural characteristics and the Late Quaternary activity of the WNF may provide for the overall study of the structural characteristics and seismic risk of the Hetao Basin as well as an essential scientific basis for urban and rural construction and land resource planning in the Hetao Basin.

As the boundary between Wulashan and the Hetao Basin, and the boundary of a stratum from the view of geomorphology and stratigraphy, separately, the WNF was inferred to be on the northern foot of Wulashan (Guo et al., 1980). However, no definitive proof exists, such as fault cliffs, triangular facets, fault scarps, or fault gouges. Owing to serious desertification and buried structural traces along the WNF, there is no systematic mapping and exploration work along the WNF, and more extensive information could be obtained. Current knowledge about this fault's distribution and the Quaternary activity mainly depends on understanding the relationship between the schistositized zone of the fault stretching west of Xiaoshanzui and overlying Quaternary flood-slope sediment. Some Chinese scholars argued that the activity of WNF has been weak since 66.78 ±5.14 ka B.P. (Chen, 2002; He et al., 2019). However, it remains uncertain the geometry of the fault and when the latest activity occurred. Therefore, it is necessary to use relevant methods of active fault exploration to conduct further research on the shallow structural characteristics and Late Quaternary activity of the WNF.

The research methods for studying the Quaternary activity of inferred or buried faults are becoming more advanced. The most commonly used and practical detection approach is based on combining the three methods of shallow artificial seismic exploration, drilling exploration, and the study of the stratigraphic age. Generally, the location of faults, burial depth of the upper breakpoints, and shallow structural morphology are obtained using shallow seismic exploration methods (He et al., 2001; Yang et al., 2004; Liu et al., 2008; Liu et al., 2009; Fang et al., 2015). Subsequently, the location of the fault and burial depth of the upper fault point are further determined by a combination of drilling and profile and stratigraphic age analyses. In addition, the latest active ages, dislocation quantities, and slip rates of the faults can be simultaneously analyzed (Xiang et al., 2003; Xu et al., 2000; Lei et al., 2008; Lei et al., 2011a; Ezquerro et al., 2015). In this study, we aimed to analyze the shallow structural morphology and Late Quaternary activity parameters of the WNF by using a combination of shallow seismic exploration and drilling joint profile detection.

2 Geological background

The east-trending Hetao Basin is located along the northern margin of the Ordos Block. It extends from 40 to 80 km from north to south and ~440 km from east to west. Controlled by the northern boundary faults, including Langshan Piedmont Fault (LPF) -Sertengshan Piedmont Fault (SPF), and Wulashan Northern Fault (WNF), Wulashan Piedmont Fault (WPF), and Daqingshan Piedmont Fault (DPF), the Hetao Basin is divided into three sags including Linhe Sag, Baiyanhua Sag, and Huhe Sag from west to east. These sags are right-step echelon arranged and dustpan-shaped, deep in the north and shallow in the south, well preserving thick Quaternary sedimentation (The Research Group on Active Fault System around Ordos Massif, 1988). According to drilling and petroleum geological profiles, the Linhe Sag in the western part of the Hetao Basin is the deepest Cenozoic basin in the Ordos Block, with a maximum thickness of 2,400 m in Quaternary (Figure 2) (Ran et al., 2003b). The prominent uplift in the basin is the Wulashan Horst.

The Cenozoic Strata of the Linhe Sag is mainly composed of the Pliocene, Middle Pleistocene, Upper Pleistocene, and Holocene sediment. The lithological characteristics of different periods are as follows:1) The Pliocene Series consist of purple-red and brick-red sandy clay rock; 2)The Middle Pleistocene is mainly composed of blue-gray sub-sandy soil and grayish-black muddy clay; and 3)The Upper Pleistocene mainly consists of a sedimentary combination of gray, yellow-green silt, fine sand, gray-brown silt mixed with gravel, clay, silt, and sandy-clay, with the lower part being lacustrine facies and the upper part being alluvial lacustrine facies. The Holocene series is composed of light greyish-yellow gravel, breccia, and sandy soil containing breccia, mainly consisting of alluvial–proluvial deposits with relatively coarse particles (Li, 2006; Fan et al., 2011; Liu et al., 2014; Bi et al., 2021). The thickness of the Quaternary in the region ranges from 400 to 2,000 m and the thinnest point is located near Xiaoshanzui, Wulateqianqi County, with a thickness of ~400 m (The Research Group on Active Fault System around Ordos Massif, 1988).

The Wulashan Horst is an E-W tectonic uplift controlled by the WNF and WPF. It is about 120 km long and 15–20 km wide in the east, narrowing westward, and pinching out at Wulateqianqi County. The activity of the WPF on the southern foot is more potent than that on the northern foot. Tectonic uplift is asymmetric in the Wulashan, and higher at the southern flank (He et al., 2019; Shi et al., 2021). The tectonic landforms, such as fault cliffs, fault triangles, and fault scarps, are clear and prominent in scale and spread continuously in front of the southern foot. In contrast, the fault cliffs and fault triangles on the northern foot are blurred because of the weaker activity of WNF (The Research Group on Active Fault System around Ordos Massif, 1988).

The WNF, taken as the boundary fault of the Wulashan Horst and Linhe Sag, plays a vital role in the seismic risk analysis of the Hetao Basin. Destructive earthquakes near the fault include the 849 A.D $M = 8.0$ and the 1996 Baotou $M = 6.4$ earthquakes (He et al., 2020). This WNF is a normal fault about 75 km long and has a northeast–east strike, northward dip, and dip angle of ~80°. It extends from Xiaoshanzui village in the Wulateqianqi County in the west to Shadegai village northwest of Baotou City in the east. It can be divided into western and eastern segments bounded by the Miligeng village according to the geomorphologic trace of the fault. The western segment's linear trace between horst and sag is evident from the remote sensing images but blurred in the eastern segment (Figure 2). From the geological map, the sag controlled by the eastern segment is less than 10 km wide and comprises scattered residual mountains of bedrock. Its surface is mainly covered by deserts without notable fault scarps and a clear structural trace in

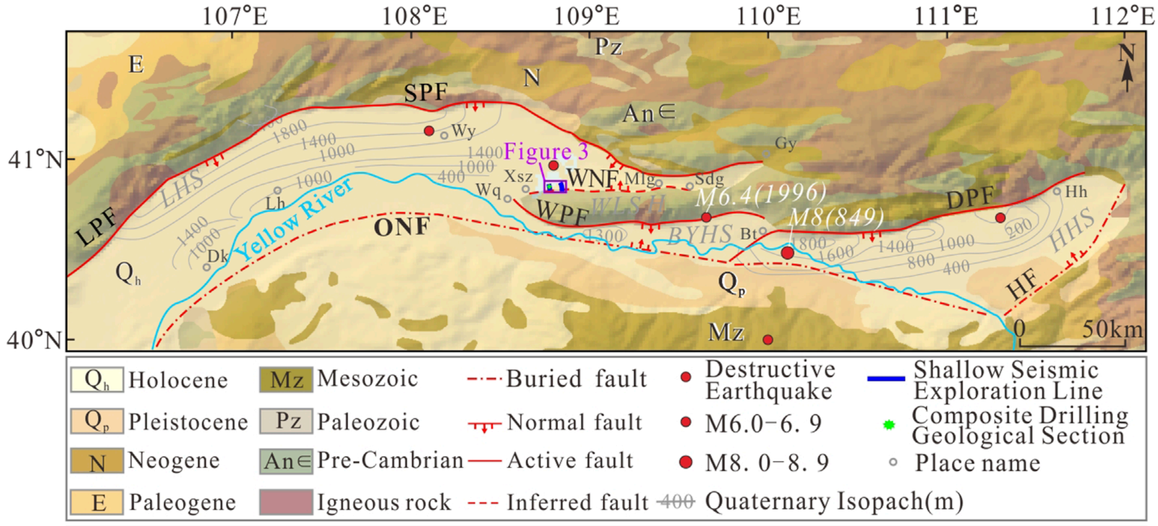

Abbreviations: WLSH, Wulashan Horst; LHS, Linhe Sag; BYHS, Baiyanhua Sag; HHS, Huhe Sag; Bt, Baotou; Hh, Hohhot; Dk, Dengkou; Lh, Linhe; Wy, Wuyuan; Xsz, Xiaoshanzui; Wq, Wulateqianqi; Mlg, Meiligeng; Sdg, Shadegai; Gy, Guyang

FIGURE 2
Seismic and geological map of the study area (See Figure 1 for location). Strata from (Zhu, 1964), Quaternary sedimentary isopaches from (Ran et al., 2003b), and epicenter of earthquakes *M* = 8.0 and *M* = 6.4 from (He et al., 2020).

Quaternary (Chen, 2002). The WNF is located in a piedmont alluvial plain area, the sedimentary facies are mainly alluvial-lacustrine. Although the sediment particles are coarse and poorly sorted, their stratification characteristics are distinct.

3 Materials and methods

3.1 Shallow seismic survey lines

Shallow seismic exploration is a geophysical method that utilizes differences in the elasticity and density of subsurface media to infer the nature and shape of subsurface rock layers by observing and analyzing the response of Earth to artificially generated seismic waves. This method can be used to detect and study the geological structure of shallow crust (Zhao et al., 2011; Yang et al., 2016). Shallow seismic exploration includes two basic methods: the refraction and reflection wave methods (Deng et al., 2003). The reflection seismic exploration method can be utilized to obtain records with a high signal-to-noise ratio and high resolution because of "small path distance, small gun distance, high coverage times" acquisition technology and high-precision data processing. Therefore, buried faults, cavities, and nonuniform anomalies can be effectively detected with the reflection seismic exploration method (He et al., 2001). At present, reflection seismic methods are widely used to detect the location, nature, and activity of the active faults with upper fault points buried more than ten to hundreds of meters deep in Quaternary overlying areas in Chinese cities, such as Fuzhou City, the capital of the Fujian Province, and Yinchuan City, the capital of the Ningxia Autonomous Region (Zhu et al., 2005; Chai et al., 2006; Li et al., 2017).

In this study, the location and shallow structural characteristics of the WNF were analyzed using shallow reflection seismic exploration. In October 2021, two shallow seismic survey lines crossing this fault named L1 and L2 were established (Figure 3A). The L1 seismic line was laid on a desert road northeast of Mostingamu village (northwest to southeast, 3.15 km long). The L2 seismic line was established on a desert road ~6 km east of L1 (southeast to northwest, 4.66 km long).

For shallow seismic exploration, 508 XT digital seismographs were used to collect field data (Figure 4A), and a P26-TYPE VIBROSEIS was employed to trigger seismic waves (Figure 4B). The basic parameters were as follows: frequency range of 20–120 Hz and scan length of 16 s. The observation system consisted of a channel spacing of 2 or 3 m, gun spacing of 10 or 15 m, and 600 or 700 channels of internal excitation and bilateral asymmetric reception. The sampling interval was 1 ms. The duration of each record was 2 s.

3.2 Composite drilling of geological sections

Composite drilling of geological sections is generally performed based on shallow seismic exploration. The drill holes were located on both sides of the fault, where geophysics indicated a clear vertical displacement. When the geophysical survey showed that the main fault was divided into several branches, composite drilling geological sections were established across the branch fault. The shallowest burial depth was the upper fault point. The borehole line coincided with, or nearly coincided with, the shallow seismic survey line and intersected the fault strike vertically or at a large angle. The drilling sequence was carried out mainly referred to the principle of the folding method, which is a construction method

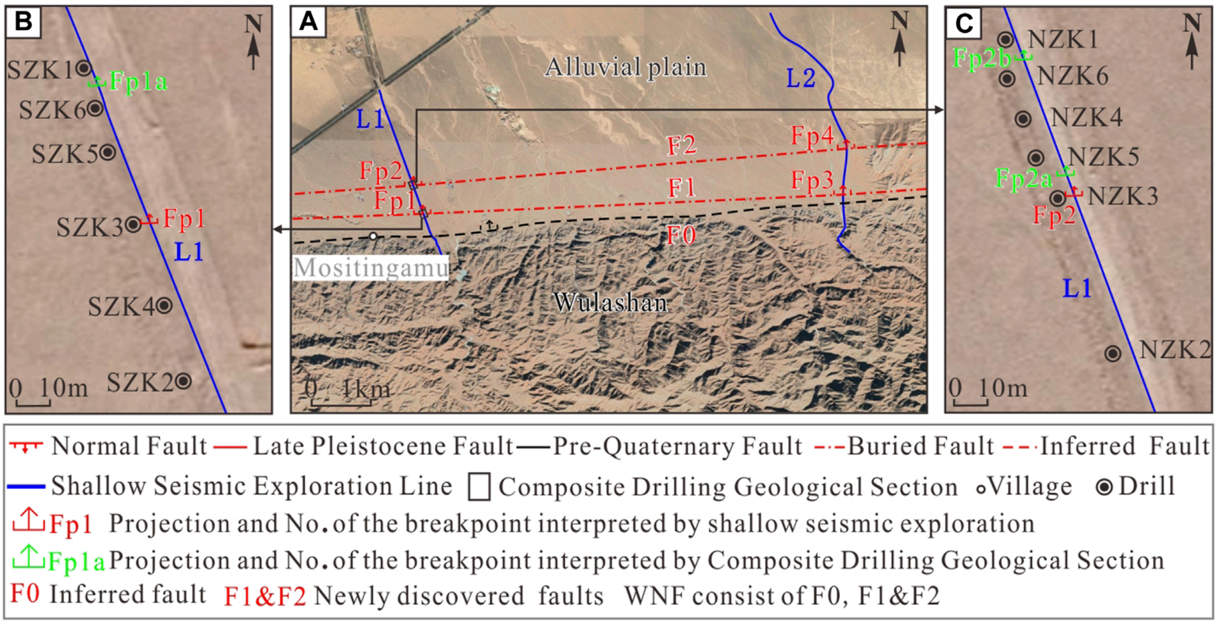

FIGURE 3
Locations of conducted shallow seismic survey lines and composite drilling of geological sections (See Figure 2 for location). **(A)** Locations of shallow seismic survey lines L1 and L2. **(B)** Location of the MSTS boreholes. **(C)** Location of the MSTN boreholes.

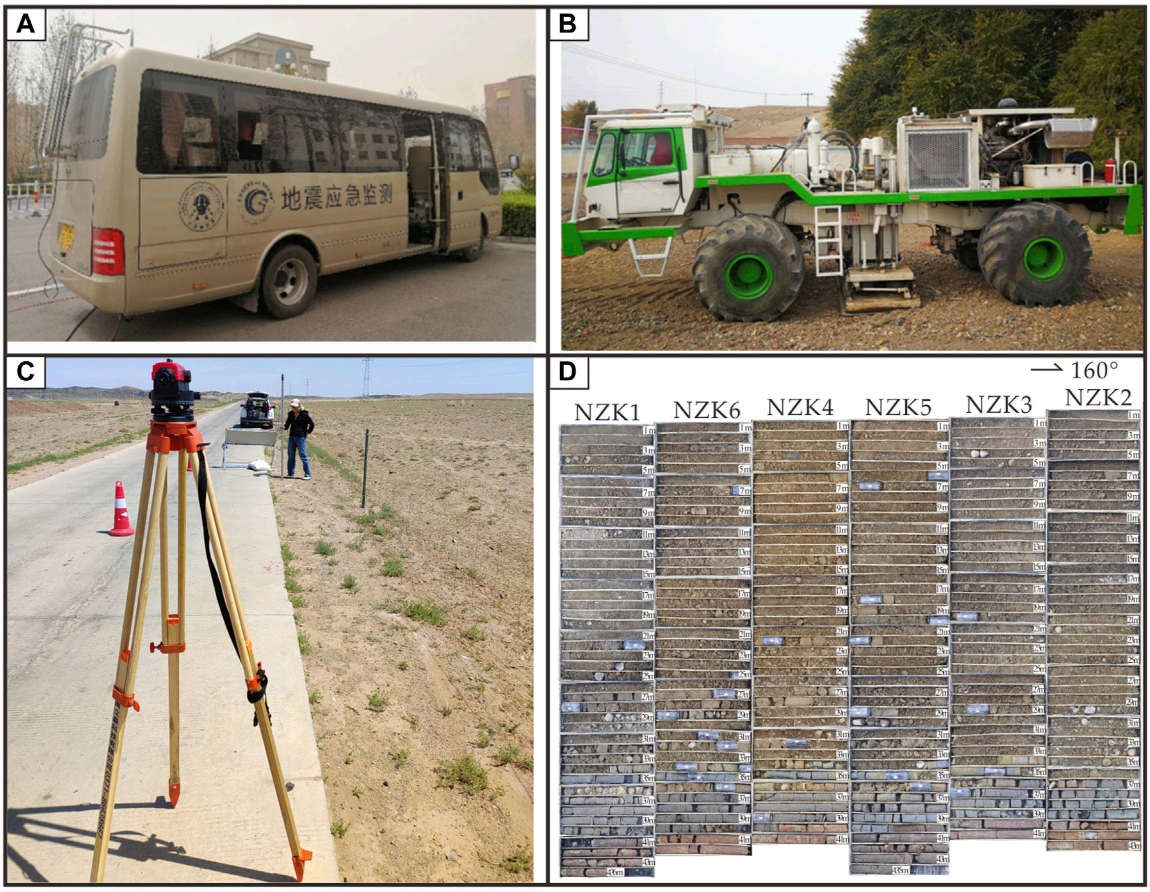

FIGURE 4
Equipment and total core recovery. **(A)** The 508 XT Digital Seismograph. **(B)** P26-TYPE VIBROSEIS. **(C)** Total station. **(D)** Core recovery percentage of MSTN sections.

of folding from the outside to the inside, gradually approaching the fault, emphasizing the dynamic construction and analysis, and continuous exclusion and determination to gradually define the location of the fault. Figure 3C represents the classical method of the folding method. Specific operation steps of this method are as follows: 1) Taking vertical projection position on the ground of the upper breakpoint Fp2 obtained by shallow artificial seismic exploration as the datum point, drill boreholes NZK1 and NZK2 at both ends of the drilling section to make sure the fault is between the two boreholes; 2) Drill the third borehole NZK3 at the middle of the two boreholes. According to the drilling results of NZK1, NZK2, and NZK3, it is concluded that the fault lies between the drilling holes of NZK1 and NZK3; 3) Continue to drill borehole ZK4 at the middle of ZK1 and ZK3. By repeating a similar practice, boreholes ZK5 and ZK6 are constructed respectively to constrain progressively the accurate fault Fp2a and Fp2b (Lei et al., 2011a). Several application cases show that the method can determine precisely the location of buried active fault (Lei et al., 2011b; Lei et al., 2014; Cao et al., 2015; Shen et al., 2022).

To further study the surface structure and active parameters of the WNF, such as the buried depth of the upper fault point and coseismic dislocation, two composite drilling geological sections were established in October 2022 based on the results of the shallow artificial seismic exploration and field survey as well as the position of the upper breakpoint of faults Fp1 and Fp2 explained by the L1 line survey using the folding method: the Mostingamu North Section (MSTN) and Mostingamu South Section (MSTS). The two sections crossed the fault and nearly coincided with the L1 shallow seismic reflection section (Figure 3A). Six boreholes were drilled in the MSTS; that is, SZK2, SZK4, SZK3, SZK5, SZK6, and SZK1 from south to north, with a borehole spacing of 25, 25, 25, 12.5, and 12.5 m, respectively (Figure 3B). The depths of the single holes were 41.5, 42, 41, 48, 41, and 42.6 m, respectively, with 256.1 m cumulative footage. Six boreholes were drilled in the MSTN; that is, NZK2, NZK3, NZK5, NZK4, NZK6, and NZK1 from south to north, with a borehole spacing of 50, 12.5, 12.5, 12.5, and 12.5 m, respectively (Figure 3C). The depths of the single holes were 43, 41, 43.5, 41, 42, and 43.6 m, respectively, with 254.1 m cumulative footage. Before analyzing the fault nature and fault characteristics of the same stratum, the relative elevation of the boreholes at the two sites was separately corrected by the total station (Figure 4C). The topography of the two combined geological sections was high in the south and low in the north. The vertical dislocation between holes SZK1 and SZK2 in the MSTS was 2.0 m. The height difference between boreholes NZK1 and NZK2 in the MSTN is 1.96 m. In addition, the back footage was controlled within 1–2 m and the core recovery percentage was greater than 95% (Figure 4D).

3.3 Sampling and testing of the stratigraphic age

Optically Stimulated Luminescence (OSL) dating is one of the most popular and accepted dating techniques in Quaternary research. The main dating materials are quartz and feldspar. The test particle sizes are generally divided into coarse, medium, and fine. The dating ranges from decades to 100,000 and more than 700,000 years (Huntley and Prescott, 2001; Liu et al., 2011; Lai et al., 2013). This technique has been widely used for sediment samples from loess, deserts, lakes, rivers, and glaciers (Fan et al., 2013; Lu et al., 2016; Wang et al., 2017; Wei et al., 2018; Zeng et al., 2019; Ou et al., 2021). The lithology of the samples collected in this study was mainly alluvial–alluvial sub-clay and alluvial–lacustrine clay. OSL dating was used to determine the absolute stratigraphic ages of the samples.

The latest activity of the fault occurred after that of the top of the latest strata deformed by the fault and before that of the bottom of overlying unfaulted strata in the combined borehole geological section. Three and two OSL dating samples were collected from the MSTS and MSTN, respectively. The lithologies of the samples mainly consist of sandy sub-clays. The collection of samples was synchronized with the collection of the drilling core and all samples were packaged in a light-proof manner.

Sample tests were conducted at the Shandong Seismological Engineering Research Institute. The tests comprised four steps: pretreatment, equivalent dose test, environmental dose rate test, and data analysis (Lu et al., 2007). The pretreatment was performed in a dark laboratory room with a light-emitting diode light source of 661 ± 15 mm. All samples were uncontaminated and unexposed at the center of the package. During pretreatment, 30% hydrogen peroxide (H_2O_2) and 30% hydrochloric acid (HCl) were added successively to remove organic matter and carbonates from the sample. Subsequently, feldspar and α-irradiated quartz surfaces were removed using40% hydrofluoric acid (HF) etching for 40 min, followed by treatment with 10% HCl to remove fluoride, ensuring that no feldspar minerals were present in the sample. The equivalent dose of all samples was measured using a Danish Risoe DA-20-C/D Thermoluminescence/Luminescence automatic measuring system and single-aliquot regenerative dose (Murry and Wintle, 2000; Murry and Wintle, 2003). The contributions of U, Th, and K, and their decay to the environmental dose rate were measured using a plasma mass spectrometer and full-spectrum plasma emission spectrometer. The effects of the moisture content and cosmic rays were considered. The sample age was equal to the equivalent dose divided by the environmental dose rate (Table 1).

4 Results

4.1 Shallow seismic reflection profile section and interpretation

4.1.1 Shallow seismic profile characteristics of survey line L1

Post-stack migration time and depth-section interpretations of line L1 are shown in Figure 5. The reflection time profile indicates multiple relatively continuous reflected wave events with a two-way travel time above 600 ms. According to the wave group characteristics of the reflection time section, three formation reflection interfaces were identified in the section, which were marked as T1, T2, and T3. The reflection energies of reflected wave events T1 and T2 are strong and continuous reflection information can be observed. South of the stake number of 5,025 m and a two-way travel time shallower than 350 ms, the reflected wave event T3 is faintly visible and can be tracked continuously. North of stake number 5,025 m and two-way travel time 400 ms deep, the reflected energy was extremely weak, and the reflected information of event T3 was almost invisible. The stratigraphic interface revealed by the seismic profile generally exhibits a shallow distribution shape in the south and is deep in the north. T2 strata are in unconformable contact with the overlying T1 strata.

Based on the transverse continuity characteristics of the reflected wave group, three secondary faults were interpreted in the section, which were marked as faults of Fp1, Fp1.1, and Fp2, respectively. The parameters for each breakpoint are listed in Table 2. The fault Fp1 is a normal fault with a northerly dip. The distinguishable upper breakpoint of the fault is located at stake number 5,470 m on the survey line and the buried depth is ~165 m. The fault Fp1.1 is a normal fault. The distinguishable upper breakpoint is located at stake number 5,230 m of the survey line, with a buried depth of ~155 m, forming an inverted Y-shape with fault Fp1. Fault Fp2 is a normal fault that dips to the north; the distinguishable upper breakpoint is located at survey line stake number 5,005 m and the buried depth is ~120 m.

4.1.2 Shallow seismic profile characteristics of survey line L2

Post-stack migration time and depth-section interpretations of the line L1 are shown in Figure 6. The reflection time profile indicates multiple relatively continuous reflected wave events with a two-way travel time above 600 ms. According to the wave group characteristics of the reflection time section, four formation reflection interfaces were identified in this section, marked as T1, T2, T3 and T4, respectively. The reflection energies of reflected wave events T1, T2, and T3 are strong, and continuous reflection information can be observed. South of stake number 4,700 m, the reflected wave event T3 is faintly visible and can be tracked continuously. North of stake number 4,700 m, a data two-way travel time shallower than 30 ms, an exploration blind spot without effective reflection information was detected. The stratigraphic interface revealed by the seismic profile generally presents a distribution that is shallow in the south and deep in the north. The T2 and T4 strata are in unconformity contact with the overlying T1 strata.

Based on the shallow seismic profile, the reflection energy of reflected wave events T2, T3, and T4 is relatively strong, with a continuous transverse direction. According to the phenomena of folds and dislocations in the reflected wave event, a total of three faults were identified in the section and marked as faults of Fp3, Fp3.1, and Fp4, respectively. The parameters for each breakpoint are listed in Table 3. The fault Fp3 staggers the bottom interface of T1, which is a normal fault. The apparent dip is northward. The distinguishable upper breakpoint was located at survey line stake number 2,450 m, with a buried depth of ~55 m. The fault Fp3.1 is a reverse normal fault on the hanging wall of fault Fp3. The fault extends upward without breaking the T4 stratum interface. The distinguishable upper breakpoint was located at stake number 2,750 m on the survey line and the buried depth was ~115 m. The fault Fp4 staggers the T4 formation interface, extends upwards, and terminates at the lower part of the T1 bottom interface. The fault Fp4 is a normal fault with an apparent northward dip. The distinguishable upper breakpoint is located at stake number 3,235 m on the survey line and the buried depth was ~104 m.

TABLE 1 OSL dating results for the MSTS and MSTN.

Drilling geological section	No.	Buried depth (m)	Sampling horizon	U (ppm)	Th (ppm)	K (%)	Water content (%)	Environmental Dose rate (Gy/ka)	Equivalent Dose (Gy)	Age (ka)
MSTN	ZK5	34.4	Bottom of stratum 5	1.9	8.4	2.3	24.7	4.4 ± 0.2	225.5 ± 9.5	73.8 ± 2.8
MSTN	ZK3	36	Top of stratum 2	1.5	9.9	2.0	17.9	3.5 ± 0.3	288.9 ± 11.3	91.2 ± 4.4
MSTS	ZK6	25.2	Top of stratum 4	1.3	7.9	2.3	31.4	2.7 ± 0.2	55.5 ± 10	19.6 ± 3.5
MSTS	ZK6	27.7	Middle of stratum 4	0.9	4.2	2.5	20.4	2.7 ± 0.3	115.5 ± 5.5	40.8 ± 2.5
MSTS	ZK6	34.4	Bottom of stratum 3	0.8	4.4	3.1	20.1	3.3 ± 0.2	196.5 ± 20.5	59.1 ± 6.2

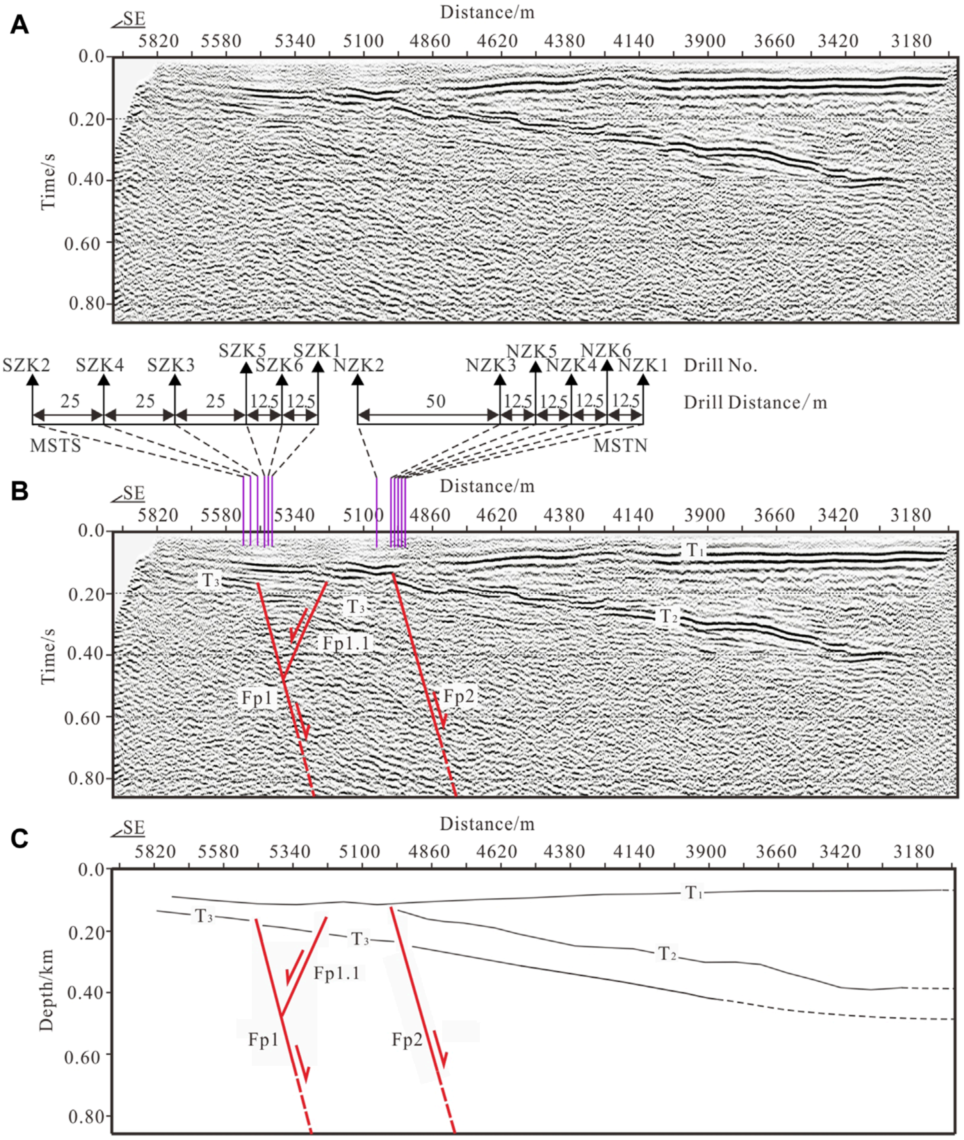

FIGURE 5
The uninterpreted and interpreted results for the L1 shallow seismic exploration profile and the layout of the boreholes. **(A)** Uninterpreted post-stack migration time-section. **(B)** Interpreted post-stack migration time-section and the distribution map of boreholes. **(C)** Depth-section interpretation.

TABLE 2 Fault parameters based on the seismic reflection profiles of L1 and L2.

No.	Breakpoint	Breakpoint Position(m)	Tendency	Buried depth (m)	Break distance (m)
L1	Fp1	5,470	N	165	5–8
	Fp1.1	5,230	S	155	2–4
	Fp2	5,005	N	120	4–7
L2	Fp3	2,450	N	55	2–4
	Fp3.1	2,750	S	115	2–4
	Fp4	3,235	N	104	3–5

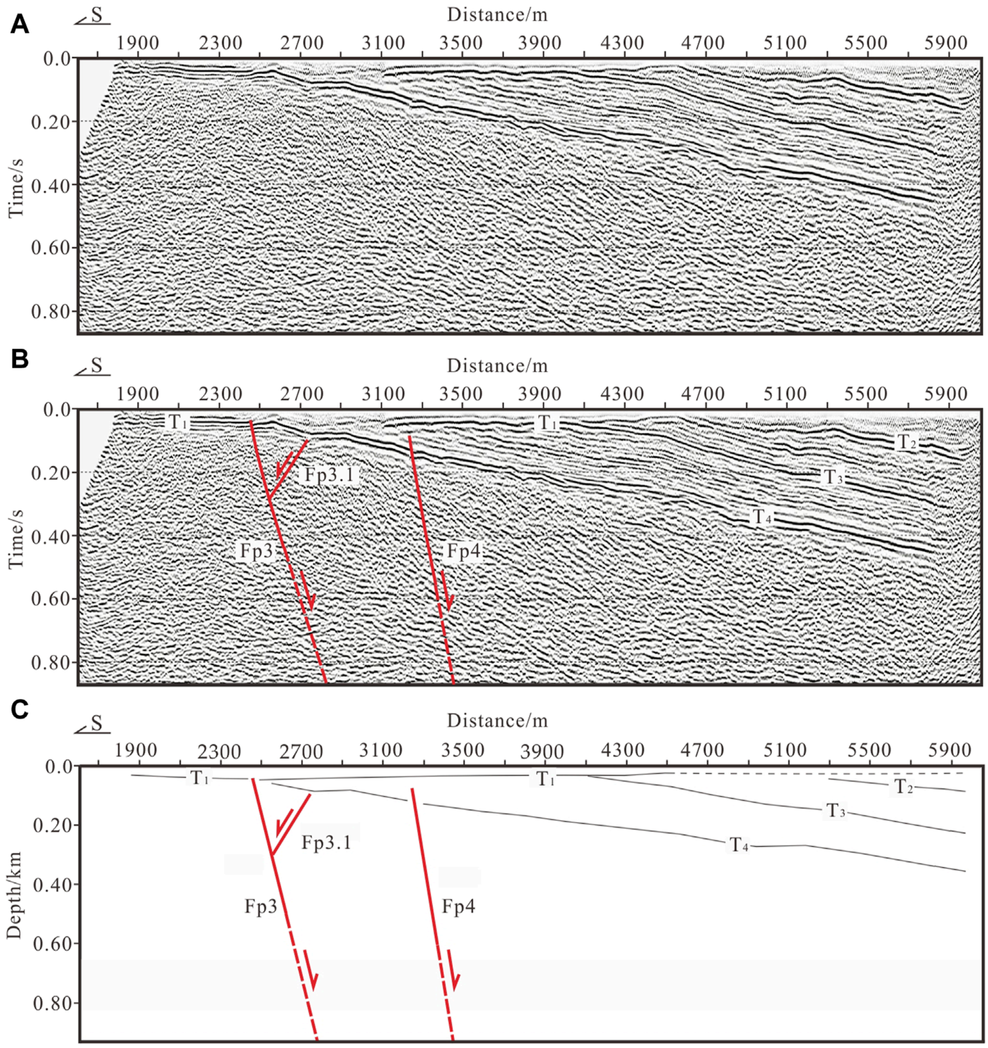

FIGURE 6
The uninterpreted and interpreted results for the L2 shallow seismic exploration profile. **(A)** Uninterpreted post-stack migration time-section **(B)** Interpreted post-stack migration time-section. **(C)** Depth-section interpretation.

Based on the comprehensive analysis of the shallow seismic exploration results of the L1 and L2 survey lines, two new faults F1 and F2 have been discovered in the northern area of Wulashan. The line connecting breakpoint Fp1 of L1 and breakpoint Fp3 of L2 is F1, and the other line connecting breakpoint Fp2 of L1 and breakpoint Fp4 of L2 is F2. Both are considered to reflect the WNF.

4.2 Geological profile detection and interpretation

The MSTS and MSTN were arranged separately across the Fp1 of F1 and Fp2 of F2 breakpoints of the WNF. Their positions in the L1 shallow seismic exploration section are shown in Figures 3, 5B.

4.2.1 Geological profile of MSTS

Based on the lithology, color, material composition, bedding structure, and other characteristics of the drilled core strata, the borehole of the MSTS section can be divided into 11 natural sublayers from bottom to top. Based on OSL dating (Table 1) and regional stratigraphy, the section can be divided into three sets of strata: Holocene (Q_h), Upper Pleistocene (Q_p^3), and Pliocene (N_2). The lithological characteristics of each layer are described in Table 3.

In the MSTS section, faults were identified in multiple strata. Our results show that strata ①, ②, and ③ underwent different degrees of structural deformation, but the top interface of stratum ④ was not affected by faults. Strata ② and ③ have a stable sedimentary thickness on both sides of the fault and their lithological characteristics significantly differ from those in the upper and lower layers, which can be used as the marker strata of fault dislocation (Figure 7A). According to the fault relationship of the strata in the same horizon, one stepped normal fault was identified, that is fault Fp1a, dipping north (Figure 8). The characteristics of the dislocation relationship between each marker layer and the fault are described in detail below.

TABLE 3 Lithological characteristics of the MSTS section.

No.	Lithology	Geological Description	Age
⑪	Loam	grayish-yellow, containing a small amount of sharp-edged gravel, with a particle size ranging from 0.2 to 0.4 cm, with poor sorting and loose structure	Q_h^{dl}
⑩	Coarse sand	yellow-brown, mixed with granite gravel, with a particle size ranging from 0.2 cm to 1.0 cm, with sharp edges and corners, with poor sorting and loose structure	Q_h^{dl}
⑨	Loam	brownish-yellow, containing blue-gray and off-white granite gravel, with a particle size ranging from 0.2 to 1.5 cm, occasionally large breccias with a particle size of 3 cm, with sharp edges and corners, with poor sorting and loose structure	Q_h^{dl}
⑧	Loam	light brown-yellow, occasionally blue-gray and off-white and light flesh-red granite gravel, particle size is concentratedat0.2–0.4 cm, occasionally clay cemented agglomerates, with poor sorting	Q_h^{dl}
⑦	Sandy Loam	light yellow-brown sandy sub-clay, containing fleshy red, gray-black, and gray granite gravels, with a particle size ranging from 0.2 to 1.0 cm, with sharp edges and corners and poor sorting, partially sandwiched with thin layers of black clay, with horizontal bedding	$Q_p^{3l\text{-}apl}$
⑥	Sandy Loam	yellowish-brown and brown with strong sandy feeling, occasionally blue gray and gray black gravel, particle size ranges from 0.2 to 3.0 cm, with sharp edges and corners and poor sorting	$Q_p^{3l\text{-}apl}$
⑤	Sandy Loam	brown-yellow, occasionally sandy glue agglomerates, containing ~10% light brick-red and gray-black granite gravel with, with sharp edges and corners, poor sorting	$Q_p^{3l\text{-}apl}$
④	Sandy Loam	yellowish-brown, relatively loose, partially granulated, containing gray and off-white granite gravel, with sharp edges and corners, particle size concentrated at 0.2–4.0 cm, with poor sorting	$Q_p^{3l\text{-}apl}$
③	Sandy Loam	brown-yellow, relatively loose, partially cemented block, can be crushed by hand, containing small particle size blue ash, light brick-red granite debris	$Q_p^{3l\text{-}apl}$
②	Silt Fine Sand	earthy yellow, slightly yellowish green, partially containing light brick-red and blue gray granite debris	$Q_p^{3l\text{-}apl}$
①	Clay Stone	light brick-red, medium weathering, mixed with a large amount of gray-green and light brick-red granite gravel, poorly rounded, particle size concentrated at 0.2–1.0 cm, with poor sorting	N_2

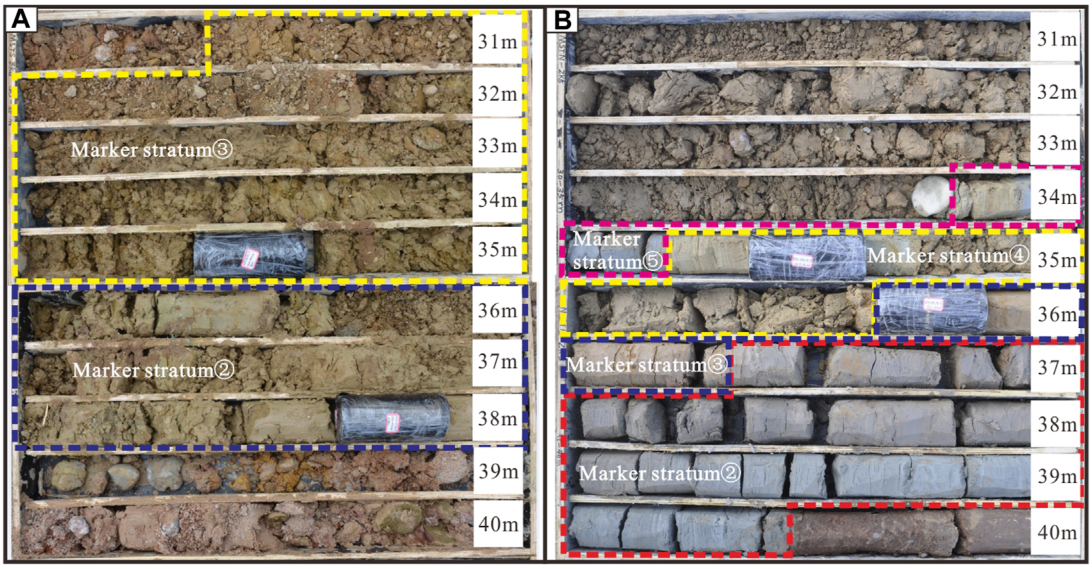

FIGURE 7
Symbolic strata of fault dislocation at the two composite drilling geological sections. **(A)** Lithology characteristics of mark stratum ② and ③ of MSTS. **(B)** Lithology characteristics of mark stratum ②, ③, ④ and ⑤ of MSTN.

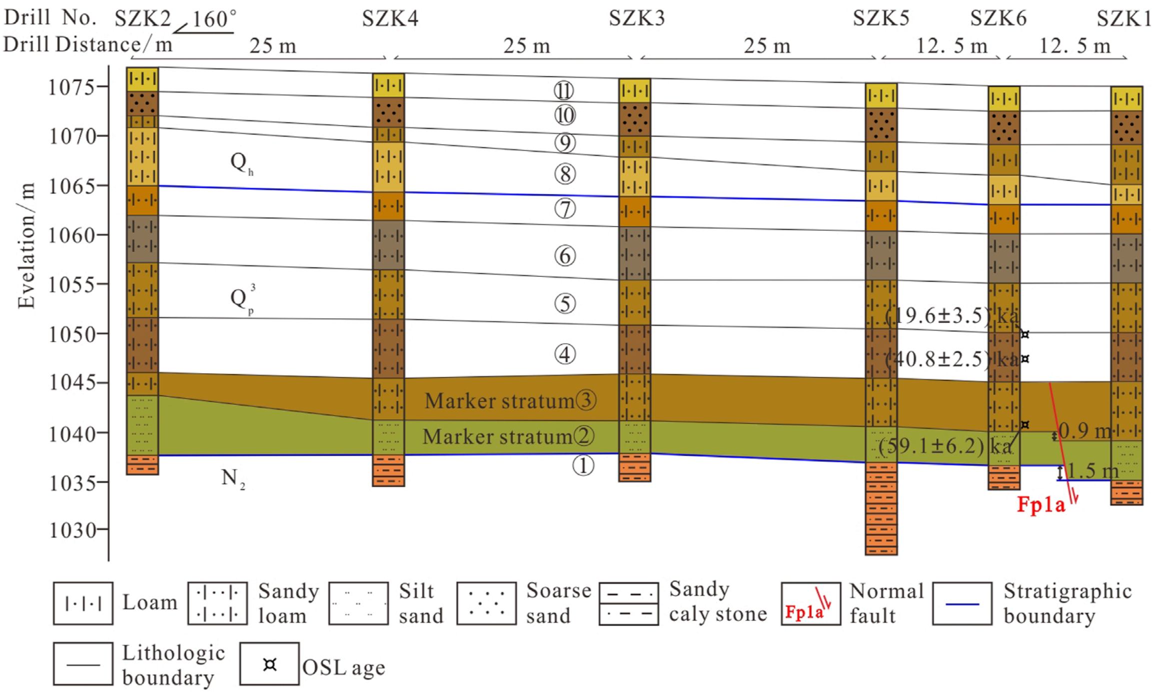

FIGURE 8
Composite drilling geological section for MSTS.

The normal fault of Fp1a was identified between boreholes ZK6 and ZK1. The formation characteristics of Fp1a are as follows: The top-bottom interface of the marker stratum ② has a notable drop on both sides of the fault Fp1a. It is characterized by a fault with thick hanging and thin footwalls. The vertical offset at the bottom interface of this layer is 1.5 m. Marker stratum ③ is brownish-yellow sandy loam, buried at a depth ranging from 33.5–36 m. The bottom interface is dislocated by the Fp1a fault between boreholes ZK6 and ZK1, with a vertical offset of 0.9 m. The top interface of marker stratum ③ is not affected by the fault and can be used as the uppermost point of the Fp1a fault, with a buried depth of ~30 m.

According to the OSL dating results of the Upper Pleistocene in the MSTS section, the stratigraphic ages at depths of 25.2, 27.7, and 34.4 m are 19.6 ± 3.5 ka B.P., 40.8 ± 2.5 ka B.P., and 59.1 ± 6.2 ka B.P., respectively. Based on these above-mentioned results, the latest activity of fault Fp1a on the F1 occurred before 40.8 ± 2.5 ka B.P.

4.2.2 Geological profile of MSTN

Based on the lithology, color, material composition, bedding structure, and other characteristics of drilled core strata, the borehole of the MSTN section was divided into 11 natural sublayers from bottom to top. Based on OSL dating results (Table 1) and regional stratigraphy, the section can be divided into three sets of strata: Holocene (Q_h), Upper Pleistocene (Q_p^3), and Pliocene (N_2). The lithological characteristics of each layer are listed in Table 4.

Results for the MSTN section show that strata ① to ④ have faults or absences in the same layers. Strata ② and ③ have a stable sedimentary thickness and notable lithological characteristics on both sides of the fault, which can be used as the symbolic strata for fault dislocation. Stratum ① is a typical ridge accumulation that can be used as a fault identification marker. Stratum ⑤ is clay, which had a relatively stable depositional environment and was deposited continuously in the five boreholes. The bottom was less deformed by the fault and can be used as a marker stratum for strata overlying the fault (Figure 7B). Based on the fault characteristics and overlying relationship of the marker layer, two stepped normal faults dipping north were identified in this section, that is, Fp2a and Fp2b (Figure 9). Dislocated marker strata are described in detail below.

The normal fault of Fp2a was identified between boreholes ZK3 and ZK5. The formation characteristics of Fp2a are as follows: Marker stratum ② is dark gray clay. Affected by Fp2a, the layer was faulted at the bottom interface between boreholes ZK3 and ZK5, resulting in a vertical fault distance of 0.94 m. Marker stratum ③ is reddish-brown clay with a vertical fault distance of 0.98 m at the bottom interface on both sides of Fp2a. The marker stratum ④ mainly contains brown-yellow and yellow-green silt, which is only visible in the hanging wall of Fp2a and absent in the footwall. It can be assumed that the upper wall layer ④ is the deposit in front of the ridge formed by the fault scarp. Marker stratum ⑤ is yellow-green clay. The top interface of this layer has large undulations and an uneven deposition thickness, which are presumed to have been scoured. The bottom interface of this layer was close to the flat and was not affected by Fp2a. Therefore, the bottom interface of layer five can be the uppermost point of fault Fp2a, with a buried depth of ~34.2 m.

The normal fault of Fp2b was identified between boreholes ZK6 and ZK1. The formation characteristics of Fp2b are as follows: Marker stratum ② on both sides of fault Fp2b shows that the thickness of the hanging wall is larger than that of the footwall, representing characteristics of a contemporaneous fault, with a 1.15 m offset in

TABLE 4 Lithological characteristics of the MSTN section.

No.	Lithology	Geological Description	Age
⑪	Sandy Loam	yellow-brown, relatively loose, containing a small amount of light fleshy red granite gravel, with a particle size ranging from 2 to 6 cm, with sharp edges and corners, partially containing thin sandwiched yellowish-brown sub-clay	Q_h^{dl}
⑩	Loam	yellowish-brown and brown, relatively loose, containing blue-gray and off-white granite gravel, with a particle size ranging from 1 to 4 cm, occasionally large breccias with a particle size of 7 cm, with sharp edges and corners, occasionally with white hyphae	Q_h^{dl}
⑨	Sandy Loam	yellow-brown, containing a small amount of blue-gray and off-white and light flesh-red granite gravel, with a particle size ranging from 2 to 6 cm, with sharp edges and corners	Q_h^{dl}
⑧	Loam	yellowish-brown and brown sub-clay, relatively loose, containing off-white and light flesh-red granite gravel, with a particle size concentration at 4–6 cm, with sharp edges and corners, partially sandwiched with thin layers of yellowish-brown sandy sub-clay sand, white hyphae can occasionally be observed	Q_h^{dl}
⑦	Loam	yellowish-brown, occasionally containing off-white and light fleshy red granite gravel, with a particle size ranging from 1 to 4 cm, thin layer of reddish-brown fine sand can occasionally be seen, partially sandwiched with a thin layer of reddish-brown clay and yellow-green, with a small amount of gray-green and brown stripes	$Q_p^{3l\text{-}apl}$
⑥	Fine sand	yellowish-brown and brown, containing a small amount of light fleshy red granite gravel, with a particle size concentration of 4–7 cm in, occasionally large breccias with a particle size reaching up to10 cm, partially sandwiched with yellowish-brown loam and reddish-brown coarse sand	$Q_p^{3l\text{-}apl}$
⑤	Clay	yellow-green, partially mixed with thin layers of blue-gray, gray-green, and rust-yellow clay, occasionally containing rust-yellow streaks, with clear horizontal bedding	$Q_p^{3l\text{-}apl}$
④	Silt Sand	brown-yellow and yellow-green, containing a small amount of cemented sandstone blocks, thin layer of brown-yellow clay on the top with very few rust-yellow and gray-green stripes, lower part is brown-yellow, yellow-green silt	$Q_p^{3l\text{-}apl}$
③	Clay	reddish-brown clay, occasionally with yellow streaks	$Q_p^{3l\text{-}apl}$
②	Clay	dark gray with a small amount of gray-black iron-manganese spots, clear horizontal bedding	$Q_p^{3l\text{-}apl}$
①	Sandy Clay Stone	purple-red and hard, with a small number of gray-green stripes and a small amount of white spots	N_2

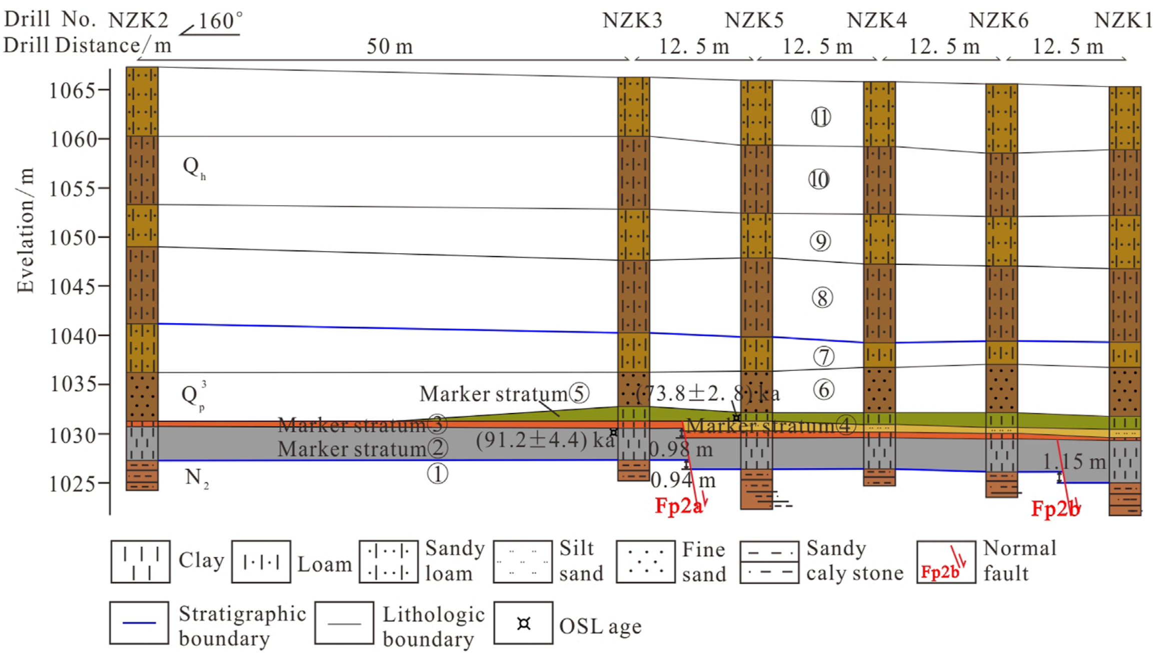

FIGURE 9
Composite drilling geological section for MSTN.

the bottom interface. Marker stratum ③ was not deformed by Fp2b. Its bottom interface can be the uppermost point of fault Fp2b, with a buried depth of ~36.3 m.

According to the OSL dating results, the geological age of the bottom interface of stratum⑤ is 73.8 ± 2.8 ka B.P. and that of the top interface of stratum ② is 91.2 ± 4.4 ka B.P. Based on these above-mentioned results, the latest activities of normal faults Fp2a and Fp2b on the F2 occurred before 73.8 ± 2. 8 ka B.P. and 91.2 ± 4.4 ka B.P., respectively.

5 Discussion

Based on the results of this detection, the WNF is not a single surface fault but rather multiple branches consisting of F0, F1, and F2. Near the surface, the three faults spread in a divergent manner to the inner terraces of the basin (Figure 3A). Faults F1 and F2 are newly confirmed late Pleistocene faults. Fault F0 must be identified from the seismic reflection profiles due to the bedrock area's lack of reflection wave groups. It is considered a pre-quaternary fault because it lacks relevant evidence of Quaternary activity.

(1) The WNF formed during the Mesozoic stage. Since the Cenozoic, the WNF has been characterized by vigorous vertical differential activity and intermittent activity, with the north wall descending and the south wall uplifting, forming an E-W trending normal slip fault zone (The Research Group on Active Fault System around OrdosMassif, 1988). In the Neogene, faults F0 and F1 dipping north and the secondary fault of Fp1.1 dipping south developed at the northern foot of Wulashan (Figure 10A). Since the Quaternary, the WNF has inherited activity. In the early and middle periods of the Late Pleistocene, a new fault of F2 developed on the northern side of F1. In the late period of the Late Pleistocene, F1 was reactivated. In the Holocene, the F1 and F2 faults were covered and turned into buried faults (Figure 10B). From the long-time scale of fault evolution, the activity of the WNF is characterized by migrating basin-ward into the hanging wall with time, which is consistent with the evolution model proposed by Dart et al. (1995).

(2) The section of MSTS crossing Fp1 on the F1 reveals one fault Fp1a with two seismic events. The latest event occurred before 40.8 ± 2.5 ka B.P., with a 0.9 m maximum coseismic dislocation. The older event occurred before 59.1 ± 6.2 ka B.P., with a 0.6 m maximum coseismic dislocation. The 1.5 m dislocation of the bottom interface of marker stratum ② was the cumulative dislocation of the two events. According to the empirical equation for magnitude and coseismic dislocation (Slemmons, 1982), considering the maximum coseismic dislocation of 0.9 m, the maximum magnitude of an earthquake on F1 can be estimated to be M = 6.63 ± 0.4, which could be the maximum probable earthquake under the condition of F1 rupture alone.

The section of MSTN crossing the branch fault Fp2 on the F2 reveals two faults Fp2a and Fp2b, with two seismic events. The latest event was the activity of Fp2a faulting simultaneously the bottom surface of maker marker stratum ② and ③ 0.94 and 0.98 m. Taking the drilling error into account, the displacement of this event is 0.96 m (average of 0.94 and 0.98 m). According to the empirical equation for magnitude and coseismic dislocation (Slemmons, 1982), the maximum magnitude of an earthquake on Fp2a can be estimated to be M = 6.65 ± 0.4. The older event was the activity of Fp2b faulting the bottom surface of maker marker stratum ② 1.15 m. According to the empirical equation for magnitude and coseismic dislocation (Slemmons, 1982), the maximum magnitude of an earthquake on Fp2b can be estimated to be M = 6.71 ± 0.4. If the F2 rupture alone, the maximum probable earthquake is between M = 6.65 ± 0.4 and M = 6.71 ± 0.4.

Suppose a full-length rupture of the WNF, the scale of the fault zone is also an important factor affecting the magnitude of the earthquake. According to the empirical equation for magnitude and length (Well and Coppersmith, 1994), the maximum possible magnitude of an earthquake related to this fault zone can be estimated to be M = 7.3 ± 0.34. However, considering estimate errors and given that the latest activity of the WNF occurred during the late stage of the Late Pleistocene, the maximum magnitude of a potential earthquake is determined to be M = 6.5–7.0.

This passage enriches the research on the Quaternary activity of boundary faults in the Hetao Basin. Summing up briefly the previous achievements: 1) The vertical activity rate of the Langshan Piedmont Fault was 1.12 mm/yr since the Holocene (Sun et al., 2021); 2) The average vertical slip rate of the Sertengshan Piedmont Fault since 65 ka was 1.8–3.2 mm/a (Liang et al., 2019); 3) the vertical slip rates of the Daqingshan Piedmont Fault were 2.5–3.88 mm/a and 1.78–2.83 mm/a since 58 and 11 ka (Xu et al., 2022); 4) the vertical slip rate of Wulashan Piedmont Fault were 2.20–2.28 mm/a and 1.12–1.34 mm/a since 65 ka and Holocene (He et al., 2020); 5) the latest activities of the WNF were 47.08 ± 3.7–73.8 ± 2.8 ka B.P. and the maximum vertical dislocation were 0.9–1.15 m; 6) the coseismic vertical displacement of the Ordos Northern Fault was 2–2.5 m, and the latest activity occurred 43.5–70 ka B.P. (Liu et al., 2022); 7) the activity of the Horiger Fault had tended to be stable since late of the Late Pleistocene (Hao, 2017). In other words, the Late Quaternary activity of the Langshan Piedmont Fault, Sertengshan Piedmont Fault, Daqingshan Piedmont Fault, and Wulashan Piedmont Fault are the most active. According to related studies, the maximum possible magnitude of the earthquake in the Langshan Piedmont Fault - Sertengshan Piedmont Fault is 8.1 (Liang et al., 2021). The Daqingshan Piedmont Fault has the highest probability of producing an earthquake with a magnitude of 7.0 or 7.5 in the next 100 years and the Wulashan Piedmont Fault is more likely to produce an earthquake with a magnitude 7.0 or more significant in the next hundred years (Pan, 2021). It suggests that future earthquake prevention and disaster reduction efforts in the Hetao Basin should be focused on those faults.

(3) According to historical records, a great earthquake M = 8.0 occurred on October 20, 849 A.D., in the Hetao Basin area causing serious destruction of civilian houses and thousands of deaths. Through reevaluating the earthquake intensity and locations of the main damaged place, Yuan et al. (2023) modified the isoseismal line, which shows that the earthquake has affected Hetao Basin and its south area with slow attenuation of seismic intensity on the south side; and attenuation of seismic intensity is fast with quite small affected area on the north side, and the WNF is located in the

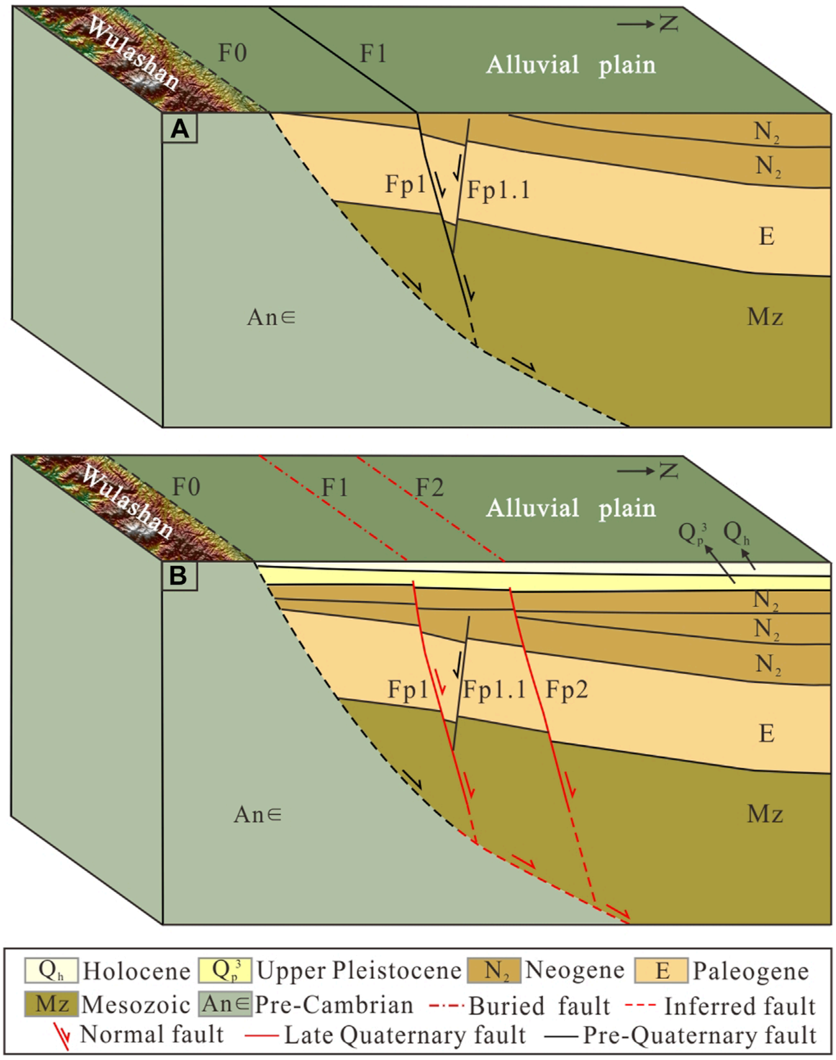

FIGURE 10
Cartoon illustration of the evolution model of the Wulashan Northern Fault. **(A)** Cartoon illustration of geological structure of the Wulashan Northern Fault in the Neogene. **(B)** Cartoon illustration of geological structure of the Wulashan Northern Fault in the Holocene.

VIII ~ IX of Intensity Zone (Figure 11). The earthquake has caused obvious surface rupture of the Daqingshan Piedmont Fault. However, we did not find any surface rupture on the WNF in the field. In addition, the latest activity of the WNF was Late Pleistocene. So, the WNF did not participate in this earthquake $M = 8.0$ in 849 A.D.

(4) Although the latest activity era of the WNF given in this article is weaker than that of adjacent faults and did not participate in the earthquake $M = 8.0$, considering the interaction between faults, that is, the rupture mechanism triggered by positive Coulomb stress (Shen et al., 2004), the WNF is located in the positive region of Coulomb Failure Stress Change (ΔCCFS) by Yinchuan-Pingluo historical earthquake of $M = 8.0$ in 1739 A.D. During the past nearly 300 years, several earthquakes with a magnitude of about $M = \sim 5$ have occurred along the Langshan Piedmont Fault and Sertengshan Piedmont Fault (Figure 2). Considering the continuous loading of coseismic and post-seismic tectonic stress, this secondary fault of WNF with a total length of 75 km has a relatively higher earthquake risk in the future which cannot be ruled out. Therefore, we should carry out more work along WNF and consider the possibility of independent rupture.

6 Conclusion

In this study, we obtained the shallow structural morphology and checked the Late Quaternary of Wulashan Northern Fault by two shallow seismic exploration profiles and two composite drilling geological cross-sections in the Hetao Basin, northern side of the Ordos Block. The following results were obtained:

(1) The Wulashan Northern Fault is a stepped northward-dipping normal fault system. Among them, the piedmont fault F0 is a Pre-Quaternary fault. Faults F1 and F2 far away from the

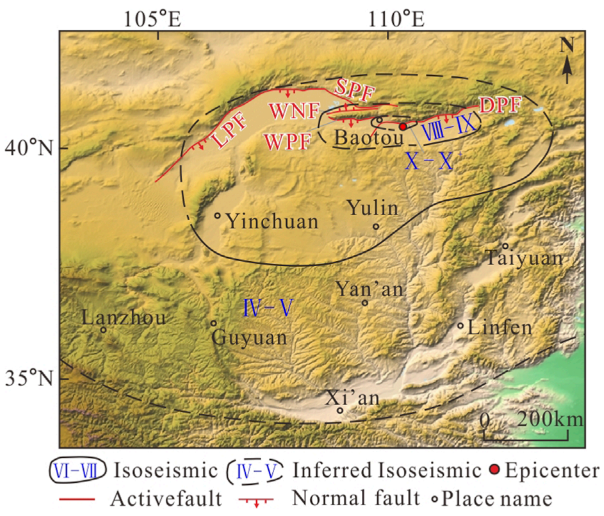

FIGURE 11
Isoseismal map of the earthquake in 849 A.D. Isoseismic lines from (Yuan et al., 2023); Location of epicenter from (He et al., 2020).

Wulashan are Late Pleistocene faults. The latest activity of the fault Fp1a on the F1 occurred before 40.8 ± 2.5 ka. The maximum vertical dislocation was 0.9 m. The latest activities of the faults Fp2a and Fp2b on the F2 occurred before 73.8 ± 2.8 ka B.P. and 91.2 ± 4.4 ka B.P., respectively, and the maximum vertical dislocation was 0.96 m and 1.15 m, correspondingly. Considering the different scenarios, the maximum magnitude of a potential future earthquake was determined to be $M = 6.5–7.0$. The Wulashan Northern Fault was not involved in the 849 A.D. $M = 8.0$ historical strong earthquake.

(2) As the Wulashan Northern Fault is located in the positive cumulative region of Coulomb Failure Stress Change (ΔCCFS) triggered by the Yinchuan-Pingluo $M = 8$ earthquake in 1739 A.D., based on statistics, there is a very high correlation between positive ΔCCFS and potential subsequent earthquakes. Although the latest activity era of the WNF belongs to the late Pleistocene, which migrated towards the basin, although it is weaker than the adjacent Holocene active faults (Langshan Piedmont Fault and Sertengshan Piedmont Fault, Daqingshan Piedmont Fault and Wulashan Piedmont Fault), further subsequent research should pay attention to its role of faulting as independent activities.

Data availability statement

The original contributions presented in the study are included in the article/supplementary material, further inquiries can be directed to the corresponding author.

Author contributions

LW: Conceptualization, Data curation, Formal Analysis, Funding acquisition, Investigation, Methodology, Software, Writing–original draft, Writing–review and editing. WH: Conceptualization, Investigation, Methodology, Project administration, Resources, Supervision, Writing–review and editing, Data curation, Formal Analysis, Funding acquisition, Software, Validation, Visualization. YX: Supervision, Validation, Visualization, Writing–review and editing. YD: Data curation, Investigation, Writing–review and editing. AD: Investigation, Writing–review and editing. XS: Investigation, Writing–review and editing. SX: Investigation, Writing–review and editing. JQ: Data curation, Writing–review and editing.

Funding

The author(s) declare that financial support was received for the research, authorship, and/or publication of this article. This research is jointly financially supported by the Spark Program of Earthquake Sciences (No. XH24054YB), Shanxi Taiyuan Continental Rift Dynamics National Observation and Research Station (Nos. NORSTY2023-03, NORSTY2021-07), and National Natural Science Foundation of China (Nos. 42041006, 42072248).

Acknowledgments

We are particularly grateful to Prof. Baojin Liu from the Geophysical Exploration Center, CEA, Prof. Yongkang Ran, Honglin He from the Institute of Geology, CEA, and Prof. Qinjian Tian from the China Earthquake Disaster Prevention Center for their helpful guidance during the field survey. We are also extremely grateful to the Shandong Institute of Earthquake Engineering for the OSL dating job.

Conflict of interest

Publisher's note

References

Bi, Z., Yang, Z., Wang, L., Ning, K., Yang, Q., and Liu, W. (2021). The sedimentary environment evolution record of QK3 borehole in Linhe depression since 220ka. *Sci. Technol. Eng.* 21 (2), 9229–9235. doi:10.3969/j.issn.1671-1815.2021.22.007

Cao, J., Ran, Y., Xu, H., Li, Y., Zhang, P., and Ma, X. (2015). Typical case analysis on application of multi-method detection technique to active fault exploration in Suqian city. *Seismol. Geol.* 37 (2), 430–439. doi:10.3969/j.issn.0253-4967.2015.02.007

Chai, C., Meng, G., Du, P., Wang, Y., Liu, B., and Shen, W. (2006). Comprehensive multi-level exploration of buried active fault: an example of Yinchuan buried active fault. *Seismol. Geol.* 28 (4), 536–546. doi:10.3969/j.issn.0253-4967.2006.04.002

Chen, L. (2002). *Paleoearthquakes, the law of strong earthquake recurrence and potential sites for the occurrence of future strong earthquakes in the Hetao fault-depression zone*. China, Beijing: Institute of Geology.

Dart, C., Cohen, H., Akyüz, H., and Barka, A. (1995). Basinward migration of rift-border faults: implications for facies distributions and preservation potential. *Geology* 23 (1), 69–72. doi:10.1130/0091-7613(1995)023<0069:bmorbf>2.3.co;2

Deng, Q., Cheng, S., Min, W., Yang, G., and Ren, D. (1999). Discussion on cenozoic tectonics and dynamics of Ordos block. *J. Geom.* 5 (3), 113–120. (In Chinese with English abstract). doi:10.3969/j.issn.1006-6616.1999.03.003

Deng, Q., Xu, X., Zhang, X., and Wang, G. (2003). Methods and techniques for surveying and prospecting active faults in urban areas. *Earth Sci. Front.* 10 (1), 93–104. doi:10.3321/j.issn:1005-2321.2003.01.012

Dong, S. (2016). *Late quaternary tectonic activity and paleoseismology along the langshan range-front fault*. China, Beijing: Institute of Geology.

Ezquerro, L., Moretti, M., Liesa, C., Luzn, A., and Simn, L. (2015). Seismites from a well core of palustrine deposits as a tool for reconstructing the paleoseismic history of a fault. *Tectonophysics* 665 (1), 191–205. doi:10.1016/j.tecto.2015.05.025

Fan, T., Fan, Y., and Wei, G. (2011). New findings and dating of lacustrine sediments in the Xishanzui subuplift, Hetao Basin. *Acta Geogr. Sin.* 66 (5), 698–708. doi:10.11821/xb201105012

Fan, Y., Chen, X., Fan, T., Jin, M., Liu, J., and Chen, F. (2013). Sedimentary and OSL dating evidence for the development of the present Hobq desert landscape, northern China. *Earth Sci.* 43, 2037–2044. doi:10.1007/s11430-013-4673-7

Fang, S., Zhang, X., Liu, B., Xu, X., Bai, D., and Ji, J. (2015). Geophysical methods for the exploration of urban active faults. *Seismol. Geol.* 24 (4), 606–613. doi:10.3969/j.issn.0253-4967.2002.04.016

Guo, J., Zhou, J., Yao, T., Song, Q., and Yang, Y. (1980). *Report on the Regional Geological Survey of the Wuyuan County, People's Republic of China (scale 1: 200,000).* doi:10.35080/n01.c.63758

Hao, L. (2017). Spatial distribution and modern activity analysis of the Horinger County Fault. *Inn. Mong. Sci. Technol. and Econ.* 24, 0052–0054.

He, C., Rao, G., Yang, R., Hu, J., Yao, Q., and Yang, C. (2019). Divide migration in response to asymmetric uplift: insights from the Wula Shan horst, North China. *Geomorphology* 339, 44–57. doi:10.1016/j.geomorph.2019.04.024

He, Z., and Ma, B. (2015). Holocene paleoearthquakes of the Daqingshan fault detected from knickpoint identification and alluvial soil profile. *J. Asian Earth Sci.* 98, 261–271. doi:10.1016/j.jseaes.2014.11.025

He, Z., Ma, B., Hao, Y., Zhao, J., and Wang, J. (2020). Surface rupture geomorphology and vertical slip rates constrained by terraces along the Wulashan piedmont fault in the Hetao Basin, China. *Geomorphology* 358, 107116–107120. doi:10.1016/j.geomorph.2020.107116

He, Z., Ma, B., and Lu, H. (2007). Active Fault segmentation and the identification of potential seismic zones along the daqingshan Piedmont Fault. *Seismol. Geol.* 29 (4), 765–775. doi:10.3969/j.issn.0253-4967.2007.04.007

He, Z., Ye, T., Ding, Z., and Sun, W. (2001). The application of shallow seismic prospecting methods to Active Fault detection in cities. *Recent Dev. World Seismol.* 3, 1–6. doi:10.3969/j.issn.0253-4975.2001.03.001

Huntley, D., and Prescott, J. (2001). Improved methodology and new thermoluminescence ages for the dune sequence in south-east South Australia. *Quat. Sci. Rev.* 20 (5-9), 687–699. doi:10.1016/S0277-3791(00)00022-6

Jiang, W., Xiao, Z., Wang, H., and Gong, F. (2001). Segmentation character of seismic surface ruptures of the piedmont active fault of Mt. Daqingshan, Inner Mongolia. *Seismol. Geol.* 23 (1), 24–34. doi:10.3969/j.issn.0253-4967.2001.01.003

Lai, Z., Mischke, S., and Madsen, D. (2013). Paleoenvironmental implications of new OSL dates on the formation of the "shell bar" in the qaidam basin, northeastern qinghai-Tibetan plateau. *J. Paleolimnol.* 51, 197–210. doi:10.1007/s10933-013-9710-1

Lei, Q., Chai, C., Du, P., Wang, Y., and Meng, G. (2011b). Activity characteristics of Luhuatai buried fault since late Quaternary revealed by drilling. *Seismol Geol.* 33 (3), 602–614. doi:10.3969/j.issn.0253-4967.2011.03.010

Lei, Q., Chai, C., Meng, G., Du, P., Wang, Y., and Xie, X. (2011a). Method of locating buried active fault by composite drilling section doubling exploration. *Seismol Geol.* 33 (1), 45–55. doi:10.3969/j.issn.0253-4967.2011.01.005

Lei, Q., Chai, C., Zheng, W., Du, P., Xie, X., Wang, Y., et al. (2014). Activity and slip rate of the northern section of Yellow River fault revealed by drilling. *Seismol Geol.* 36 (2), 464–477. doi:10.3969/j.issn.0253-4967.2014.02.015

Lei, G., Chai, C., Meng, G., Du, P., Wang, Y., Xie, X., et al. (2008). Composite drilling section exploration of Yinchuan buried fault. *Seismol. Geol.* 30 (1), 250–263. doi:10.3969/j.issn.0253-4967.2008.01.018

Li, J. (2006). *A study on the lake forming environment and tectonic activity during the Late Quaternary in the Hetao basin, Inner Mongolia Autonomous Region, China*. China, Beijing: Institute of Geology.

Li, Y. (2014). *Structural assemblages and response to strong earthquake of severali basins around the Ordos block*. China, Beijing: Institute of Geology.

Li, Y., Liu, B., Feng, S., Ji, J., Qin, J., and Guo, X. (2017). Exploration of shallow structure and buried faults in the Yinchuan basin using seismic refraction and reflection data. *Chin. J. Geophys.* 60 (8), 3096–3109. doi:10.6038/cjg20170817

Li, Y., Ran, Y., Chen, L., Wu, F., and Lei, S. (2015). The latest surface rupture events on the major active faults and great historical earthquakes in Hetao fault-depression zone. *Seismol Geol.* 37 (1), 110–125. doi:10.3969/j.issn.0253-4967.2015.01.009

Liang, K., He, Z., Ma, B., Tian, Q., and Liu, S. (2021). Joint-rupture pattern and newly generated structure of fault intersections on the northern margin of the Linhe Basin, northwestern Ordos Block, China. *Tectonics* 40, e2021TC006845. doi:10.1029/2021TC006845

Liang, K., Ma, B., Tian, Q., and Liu, S. (2019). Tectonic evolution of the turning point of the eastern and western section of the sertengshan Piedmont Fault. *Technol. Earthq. Disaster Prev.* 14 (3), 600–616.

Liu, B., Chai, C., Feng, S., Zhao, C., and Yuan, H. (2008). Seismic exploration method for buried fault and its upbreakpoint in Quaternary sediment area: an example of Yinchuan buried active fault. *Chin. J. Geophys.* 51 (5), 1475–1483. doi:10.3321/j.issn:0001-5733.2008.05.021

Liu, B., Kou, K., Hu, P., Chen, Y., Zhang, X., and Feng, S. (2009). The crustal shallow structures and buried active faults revealed by seismic reflection profiles in northwestern area of Beijing plain. *Chin. J. Geophys.* 52 (8), 2015–2025. doi:10.3969/j.issn.0001-5733.2009.08.009

Liu, H., Jia, Q., and Gong, F. (2022). Late quaternary activity characteristics of tuoketuo section of the Ordos Northern Fault. *Technol. Earthq. Disaster Prev.* 17 (2), 242–251. doi:10.11899/zzfy20220205

Liu, X., Lai, Z., Madsen, D., Yu, L., Liu, K., and Zhang, J. (2011). Lake level variations of Qinghai Lake in northeastern Qinghai-Tibetan Plateau since 3.7 ka based on OSL dating. *Quat. Int.* 236, 57–64. doi:10.1016/j.quaint.2010.08.009

Liu, Z., Zhao, H., Wang, C., Ji, Y., Zhang, Y., and Liu, L. (2014). OSL ages of sedimentary layers in Linhe depression since late Pleistocene. *Arid. Land Geogeraphy* 37 (3), 439–446. doi:10.13826/j.cnki.cn.65-1103/x.2014.03.004

Lu, H., Zhou, Y., Mason, J., Stevens, T., Yi, S., and Swinehart, J. (2016). Late quaternary climatic changes in northern China-new evidences from sand dune and loess records based on optically stimulated luminescence dating. *Quat. Sci.* 26 (6), 888–894. doi:10.3321/j.issn:1001-7410.2006.06.002

Lu, Y., Wang, X., and Wintle, A. (2007). A new OSL chronology for dust accumulation in the last 130,000yr for the Chinese Loess Plateau. *Quat. Res.* 67, 152–160. doi:10.1016/j.yqres.2006.08.003

Ma, B., Li, K., and Wu, W. (2000). "Late quaternary activities of the wulashan Piedmont Fault," in *Institute of crustal dynamics, China earthquake administration. Editors crustal. Tectonics and crustal* (Beijing, China: Seismological Press), 53–59.

Ma, B., Sheng, X., Zhang, S., and Li, Y. (1998). "Late quaternary activities of the wulashan Piedmont Fault," in *Institute of crustal dynamics, China earthquake administration. Editors crustal. Tectonics and crustal* (Beijing, China: Seismological Press), 22–27.

Ma, H., and Dong, S. (2024). A case of paleoseismic evidence of normal fault capable of triggering an M > 8 earthquake-study on Sertengshan range-front fault, north margin of Hetao Basin, China. *J. Struct. Geol.* 184 (2024), 105145. doi:10.1016/j.jsg.2024.105145

Murray, A., and Wintle, A. (2000). Luminescence dating of quartz using an improved single-aliquot regenerative-dose protocol. *Radiat. Meas.* 32, 57–73. doi:10.1016/S1350-4487(99)00253-X

Murray, A., and Wintle, A. (2003). The single aliquot regenerative doseprotocol: potential for improvements in reliability. *Radiat. Meas.* 37, 377–381. doi:10.1016/S1350-4487(03)00053-2

Nie, Z. (2013). Preliminary investigation on the historical M8 earthquake occurred in 7 BC at Baotou, Inner Mongolia. *Acta Seismol. Sin.* 35 (4), 584–603. doi:10.3969/j.issn.0253-3782.2013.04.013

Nie, Z., Ren, Y., Liu, Z., Du, C., and Cong, P. (2011). Preliminary study on seismic active faults of the Daqingshan frontal fault in Baotou City, Inner Mongolia. *Geosciences* 25 (5), 938–957. doi:10.3969/j.issn.1000-8527.2011.05.015

Nie, Z., Wu, W., and Ma, B. (2010). Surface rupture of the A.D. 849 earthquake occurred to the east of Baotou City, China, and discussion on its parameters. *Acta Seismol. Sin.* 32 (1), 94–107. doi:10.3969/j.issn.0253-3782.2010.01.011

Ou, X., Zeng, L., Chen, R., and Yao, P. (2021). Luminescence dating of glacial sediments:sampling strategies and measuring choices. *J. Glaciol. Geocryol.* 43 (3), 756–766. doi:10.7522/j.issn.1000-0240.2021.0017

Pan, B. (2021). *Research on seismic hazard evaluation of active faults on the North boundary of the Hetao fault-depression zone*. China, Beijing. China University of Geosciences.

Ran, Y., Chen, L., Yang, X., and Han, Z. (2003b). Recurrence characteristics of late-quaternary strong earthquakes on the major active faults along the northern border of Ordos block. *Sci. China D. Earth Sci.* 33 (l), 135–143. doi:10.3321/j.issn:1006-9267.2003.z1.015

Ran, Y., Zhang, P., and Chen, L. (2003a). Research on the completeness of paleoseismic activity history since Quaternary along the Daqingshan piedmont fault in Hetao depression zone, North China. *Earth Sci. Front.* 10 (l), 207–215. doi:10.3321/j.issn:1005-2321.2003.z1.029

Ran, Y., Zhang, P., Hu, B., and Guo, W. (2002). Paleoseismic activity on the Hohhot segment of Daqingshan piedmont fault in the late Quaternary history. *Earthq. Res. China.* 18 (1), 15–27. doi:10.3969/j.issn.1001-4683.2002.01.002

Rao, G., Chen, P., Hu, J., Yu, Y., and Qiu, J. (2016). Timing of Holocene paleo-earthquakes along the langshan Piedmont Fault in the western Hetao graben, North China: implications for seismic risk. *Tectonophysics* 677, 115–124. doi:10.1016/j.tecto.2016.03.035

Rao, G., He, C., Chen, P., Wu, Z., Hu, J., and Yao, Q. (2019). Active normal faulting along the seerteng Shan, North China: geometry and kinematics. *J. Asian Earth Sci.* 184 (15), 103976. doi:10.1016/j.jseaes.2019.103976

Shen, J., Dai, X., Xiao, C., Jiao, X., Bai, Q., Deng, M., et al. (2022). Study on the late Quaternary activity of the west Xiadian fault in Beijing plain. *Seismol Geol.* 44 (4), 909–924. doi:10.3969/j.issn.0253-4967.2022.04.006

Shen, Z., Wan, Y., Gan, W., Li, T., and Zeng, Y. (2004). Crustal Stress evolution of the last 700 years in North China and earthquake occurrence. *Earthq. Res. China* 20 (3), 211–228. doi:10.3969/j.issn.1001-4683.2004.03.001

Shi, F., Tan, X., Zhou, C., and Liu, Y. (2021). Impact of asymmetric uplift on mountain asymmetry: analytical solution, numerical modeling, and natural examples. *Geomorphology* 389, 107862. doi:10.1016/j.geomorph.2021.107862

Slemmons, D. (1982). Determination of design earthquake magnitudes for microzonation. *3re Int. Earthq. Microzonat. Conf. Proc.* 1, 119–130.

Su, P., He, H., Liu, Y., Shi, F., Granger, D., Kirby, E., et al. (2023). Quantifying the structure and extension rate of the linfen basin, Shanxi Rift System since the latest miocene: implications for continental magma-poor rifting. *Tectonics* 42, e2023TC007885. doi:10.1029/2023TC007885

Su, P., He, H., Tan, X., Liu, Y., Shi, F., and Kirby, E. (2021). Initiation and evolution of the Shanxi Rift System in NorthNorth China: evidence from low-temperature thermochronology in a plate reconstruction framework. *Tectonics* 40, e2020TC006298. doi:10.1029/2020TC006298

Sun, C., Li, D., and Li, L. (2021). The paleoearthquakes of the langshan Piedmont fault, North China since late Pleistocene. *Nat. Hazards Res.* 1, 48–62. doi:10.1016/j.nhres.2021.06.005

The Research Group on Active Fault System around Ordos Massif, SSB (1988). *Active Fault system around Ordos Massif*. Beijing: Seismological Press.

Wang, Q., Zhang, P., Freymuller, J., Bilham, R., Larson, K., Lai, X., et al. (2001). Present-day crustal deformation in China constrained by global positioning system measurements. *Sci.* 294, 574–577. doi:10.1126/science.1063647

Wang, S., Wang, X., and Kang, S. (2017). Luminescence dating of the last glacial Songyuan loess in northeastern China and its paleoclimate significance: preliminary results. *J. Earth Environ.* 8 (5), 397–406. doi:10.3321/j.issn:1001-7410.2006.06.002

Wei, L., Jiang, H., He, H., Xu, Y., Gao, W., and Wei, Z. (2018). Heinric-5 Event revealed by high-resolution grain-size and magnetic susceptibility records and its significance of climate evolution in the last glacial at Hongtong, Shanxi, China. *Mar. Geol. and Quat. Geol.* 38 (4), 193–202. doi:10.16562/j.cnki.0256-1492.2018.04.017

Well, D., and Coppersmith, K. (1994). New empirical relationships among magnitude, strong rupture strong length, rupture width, rupture area, and surface displacement. *B Seismol. Soc. Am.* 84 (4), 974–1002. doi:10.1007/BF00808290

Xiang, H. (2003). Some problems in the exploration and research of buried active fault. *Seismol. Geol.* 25 (3), 460–466. doi:10.3969/j.issn.0253-4967.2003.03.011

Xu, D., He, Z., Ma, B., Long, J., Zhang, H., and Liang, K. (2022). Vertical slip rates of normal faults constrained by both fault walls: a case study of the Hetao Fault System in northern China. *Front. Earth Sci.* 10, 1–19. doi:10.3389/feart.2022.816922

Xu, X., Ji, F., Yu, G., Chen, W., Wang, F., and Jiang, W. (2000). Reconstruction of paleoearthquake sequence using stratigraphic records from drill logs: a study at the Xiadian Fault, Beijing. *Seismol. Geol.* 22 (1), 9–19. doi:10.3969/j.issn.0253-4967.2000.01.002

Yang, X., Li, D., Zhao, C., Liu, B., Sun, Z., and Zhao, J. (2004). The movement age of hidden fault and analysis of width of its effect zone from shallow seismic sounding and drilling data. *Acta Seismol. Sin.* 26 (1), 88–95.

Yang, X., Liu, B., Zhan, Y., Ji, J., Xu, X., and Feng, S. (2016). Survey of crustal structure and fault activity around southern Shijiazhuang in the eastern margins of Taihangshan Mts. *Chin. J. Geophys.* 59 (2), 528–542.

Yang, X., Ran, Y., Hu, B., and Guo, W. (2002). Active Fault and paleoearthquakes of the Piedmont Fault (Wujumengkou-Dongfeng village) for seertang mountains, inner Mongolia. *Earthq. Res. China* 18 (2), 127–140. doi:10.3969/j.issn.1001-4683.2002.02.002

Yang, X., Ran, Y., Hu, B., and Guo, W. (2003). Paleoseismic activity on wujiahe segment of serteng piedmont fault, inner monglia. *Acta Seismol. Sin.* 25 (1), 62–71. doi:10.3321/j.issn:0253-3782.2003.01.008

Yuan, D., Lei, Z., Si, G., Liu, X., Yu, J., and Li, H. (2023). Supplementary research on the Baotou, inner Mongolia earthquake in 849 A. D. *China Earthq. Eng. J.* 45 (3), 501–512. doi:10.20000/j.1000-0844.20230202002

Zeng, L., Ou, X., Chen, R., and Lai, Z. (2019). OSL dating on glacial sediments of the last glacial in headwater of urumqi river, tianshan mountains. *J. Glacial. Geocryol.* 41 (4), 761–769. doi:10.7522/j.issn.1000-0240.2019.1014

Zhang, P., Burchfiel, B., Molnar, P., Zhang, W., Jiao, D., Deng, Q., et al. (1990). Late cenozoic tectonic evolution of the ningxia-hui autonomous region, China. *Geol. Soc. Am. Bull.* 102, 1484–1498. doi:10.1130/0016-7606(1990)102<1484:lcteot>2.3.co;2

Zhang, P., Deng, Q., Zhang, G., Ma, J., Gan, W., Min, W., et al. (2003). Active tectonic blocks and strong earthquakes in the continent of China. *Sci. China Earth Sci.* 46 (Supplement), 13–24. doi:10.1360/03dz0002

Zhang, X., Wang, Y., Du, P., Lei, Q., and Xie, X. (2006). Investigation about buried depth of up-breakpoint on the normal buried growth fault: Taking bore hole composite profile of buried fault in Yinchuan as an example. *Earthq. Res. China.* 22 (4), 373–381.

Zhao, C., Liu, B., and Ji, J. (2011). The acquisition technique of high-resolution seismic data for prospecting of active faults. *Technol. Earthq. Disaster Prev.* 6 (1), 18–25. doi:10.3969/j.issn.1673-5722.2011.01.002

Zhu, J., Huang, Z., Xu, X., Zheng, R., Fang, S., Bai, D., et al. (2005). Active faults exploration and seismic hazard assessment in Fuzhou city. *Earthq. Res. China.* 21 (1), 1–16. doi:10.3969/j.issn.1001-4683.2005.01.001

Zhu, X. (1964). Data from: geological map of inner Mongolia autonomous region (scale 1:1000,000). National geological data Museum (1964).